Chapter-3

CHAPTER 3: Study of Hysteresis in Centrosymmteric Copper Lead Iodide

Hysteresis in centrosymmetric $CuPbI_3$ perovskite halide: apolar dielectric or orientable dielectric? ***Prem C. Bharti****, Pardeep K. Jha, Priyanka A. Jha and Prabhakar Singh, Journal of Physics: Condensed Matter 33 (15), 155703 (2021)*

CHAPTER 3: Study of Hysteresis in Centrosymmetric Copper Lead Iodide

3.1 Introduction

It has been discussed in first chapter , perovskites halide are polar compounds which show lattice polarization effects caused by strain through electric field generation the stability issues are major problems in the Perovskite halide materials. In this chapter the aim is to study the change in polarization behavior at the surface or interface before and after light through Havriliak -Negami equation of lesser known $CuPbI_3$. In this $CuPbI_3$ synthesized through cold sintering techniques and the polarization mechanism are altered by increasing the cold sintering temperature.

We have observed the hysteresis area and shape of I-V curve in AM 1.5 G sunlight shows the drastic variation with the change in polarization behavior. Experiment suggest that apolar dielectric behavior is the cause of I-V hysteresis.

3.2 Experimental Details

The powder sample of $CuPbI_3$ was prepared by cold-sintering (solid state reaction) technique at room temperature. The precursor PbI_2 was synthesized in our lab for this the powder of lead nitrate $Pb(NO_3)_2$ and potassium iodide (KI) were taken in stoichiometric ratio. These two powders were mixed with distilled water in separate beakers. Both the solutions were heated up to 100℃ at hot plate with the constant stirring rate 550 RPM. After that, both the solutions were mixed in new beaker and put for the natural cooling. After natural cooling yellow precipitate of PbI_2 was formed, this precipitate was filtered and heated in vacuum oven for the 2 h at 100 ℃. In CS–SSR technique, PbI_2 and CuI (M/s Alfa Aesar, 99.9%) were mixed in stoichiometric ratios and ground in mortar pestle for 2 h in ambient environment and finally we get pale yellow colour powder of $CuPbI_3$. Further, powder was pelletized using hydraulic press at a pressure of 5 tons and sintered at different temperatures i.e. (i) 5℃ in ice bath at refrigerator (b) RT (30 ℃) (c) 100℃ (vacuum oven), (d) 150℃ (vacuum oven) and (e) 200℃ (vacuum oven).

The x-ray diffraction (XRD) of the pellet samples was done by using Rigaku Miniflex in the range of $2\theta = 5° – 120°$ at the step of 2 °/min. The SEM micrographs, EDX and electron back scattered diffraction image were studied using ZEISS EVO MA-15/18. The band gap was analysed using optical absorption spectrum measured by JASCO V-770 ultraviolet-visible (UV) spectrometer. The I–V measurement (room temperature, 300 K) was obtained by using Keithley 2450 source metre in dark and on the exposure to the radiation through Science tech solar simulator class: AAA with AM 1.5 G in transverse mode at a fixed scan rate of 1.66 V s^{-1} in dual sweep mode from −10 V to 10 V. Further, the impedance measurement of the studied samples is done before and after exposure of light using Solartron 1260 A impedance analyzer at different oscillation amplitudes ranging from 0.125 V to 1 V at the steps of 0.125 V.

3.3 Results and Discussion

3.3.1 X-ray Diffraction and microstructural studies

$CuPbI_3$, is lesser known perovskite with (almost) unidentified structure [199][200][201]. The materials is reported first time in 1987 by Kuku et.al [199][201] in the search of materials with ionic conduction, however recently it is also reported for its application in water splitting [200][. In these studies [199][200][201][202], authors only able to identify the hexagonal structure of $CuPbI_3$ at room temperature. In the present work, we synthesize $CuPbI_3$ with the objective to study the effect of grain size variation on hysteresis.

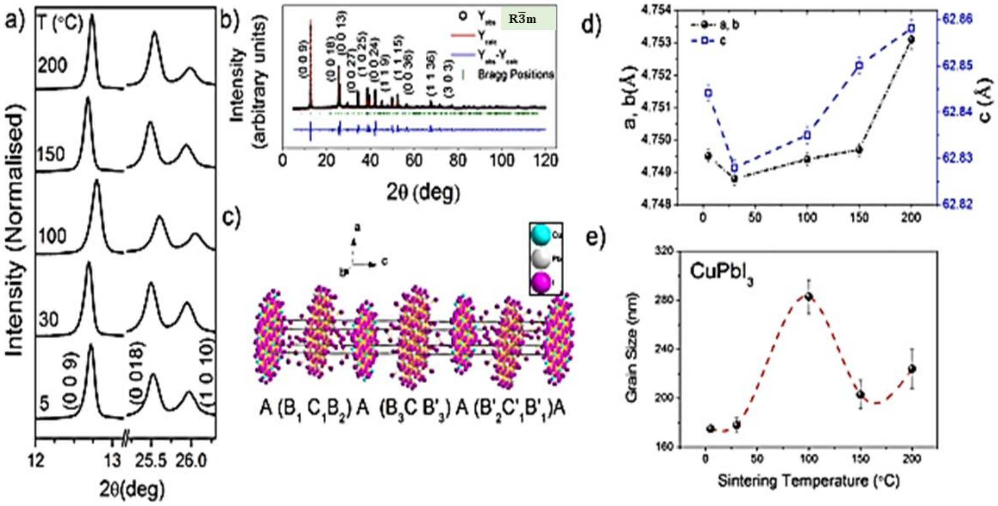

Figure 3.1 (a) XRD pattern of sample sintered at 5, 30, 100, 150 and 200 ◦C (abbreviated as T1, T2, T3, T4 and T5 respectively), (b) Le-bail fit of XRD of T3 sample with R3m symmetry (major peaks indexed), (c) 21R prototype of the R3H layered hexagonal crystal structure, (d) Variation of lattice parameters a, b and c with the sintering temperature and (e) Variation of grain size with the sintering temperature.

For this purpose we prepared the sample by cold sintering (low temperature solid state reaction) at different sintering temperatures 5, 30, 100, 150 and 200 ℃ and thereafter, abbreviated as T1, T2, T3, T4 and T5 respectively. The XRD patterns are observed to be similar to earlier reports [199][200][201][202]. The peaks with maximum intensity are plotted [Figure 3.1(a)]. However, the lack of any existing knowledge of crystalline phase makes the peak indexing work a little bit difficult. The peak indexed in earlier two works [199][200][201][202] hinting tetragonal or orthorhombic phase not hexagonal as mentioned. Thus, we took help of Raman spectra refer to Figure (3.2), which was almost similar to rhombohedral phase, so we could pin the four crystalline phases R3c, R3̄c, R3m and R3̄m.

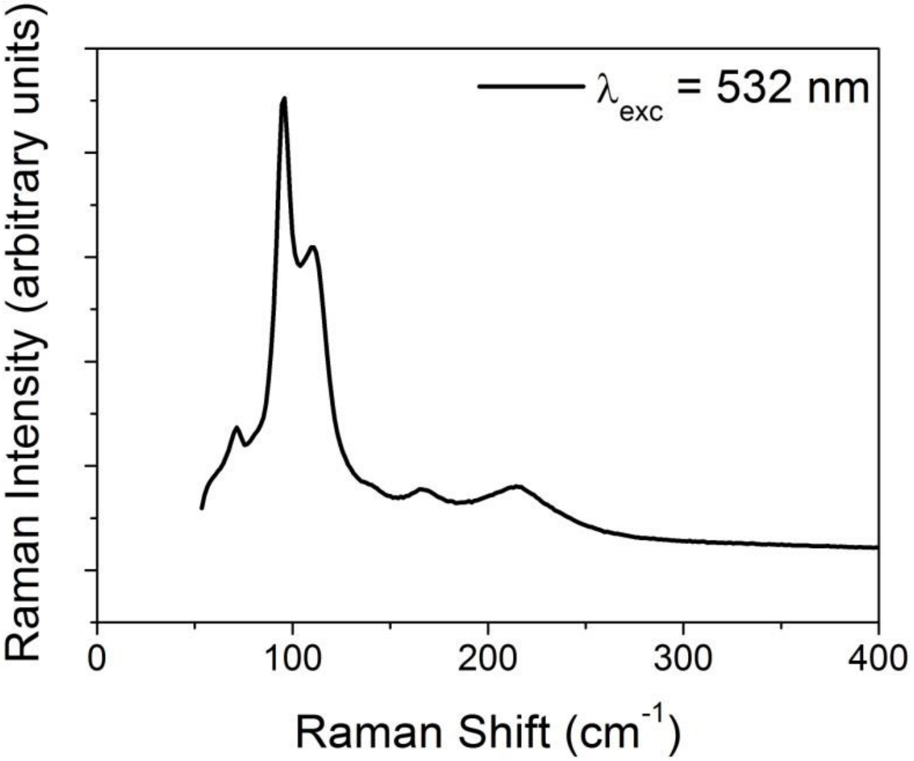

Figure 3.2 Raman spectra of powder CuPbI3 synthesized at RT with wavelength λ_{exc} = 532 nm.

Further, on applying Le-bail fits using least square refinement, the XRD pattern got fitted and indexed with hexagonal R$\bar{3}$m [Figure 3.1(b)] symmetry (lattice parameters with s.u. values a = b = 4.751(2) Å and c = 62.865(16) Å) (Le-bail fit of the $CuPbI_3$ sample synthesized at different sintering temperature is shown in Figure (3.3). This is in the partial agreement with the previous works [199][200][201][202] as it is hexagonal structure, however with different indexing [Figure 3.1(a)]. Further, we found that the present reflections comprise of −h + k + l = 3n and the absent reflections followed −h + k + l = 3n, indicating Rhombohederal symmetry (R$\bar{3}$m) [203].

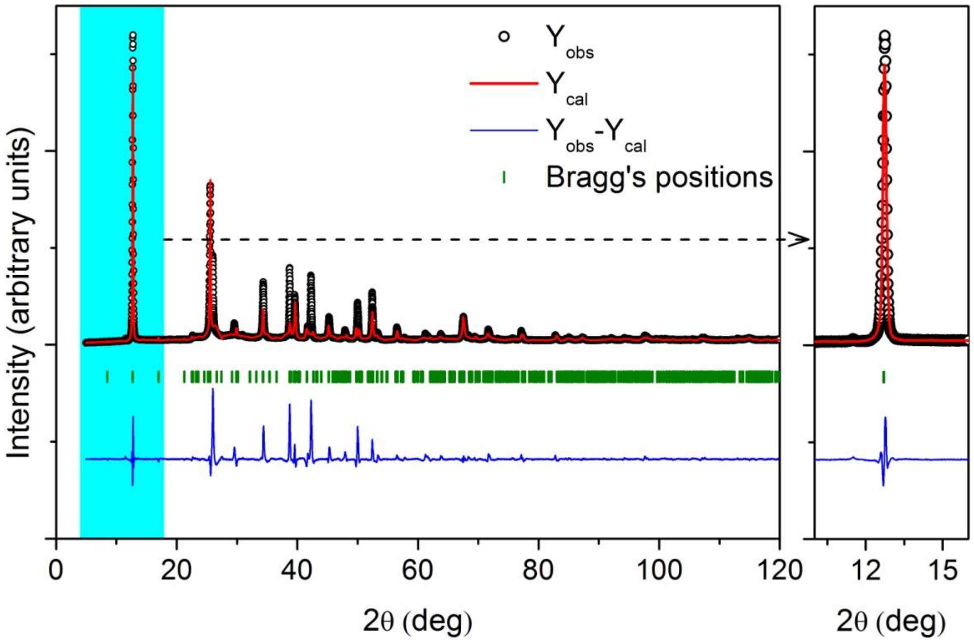

Figure 3.3 Rietveld refined spectrum of X-ray diffractograms of $CuPbI_3$ synthesized at 100 ℃ with $R\bar{3}m$ symmetry.

Since $R\bar{3}m$ symmetry possesses octahederal coordination and a set of various atomic positions were used (refer to Table 3.1). But, refinement could not be achieved giving very bad correspondence to XRD pattern. Further, face sharing octahedra and trigonal prismatic positions were also applied corresponding to other symmetries but again failed as shown in Table 3.1. Through Bilbao crystallographic server, the atomic positions were taken in a combination of 3a, 3b, 6c, 18f , 18g, 18h and 36i. In this case, refinement achieved giving better correspondence to the XRD pattern with R_f and Bragg factors of ∼6 and 7 respectively as represented in Figure 3.3, and Table 3.2. The Rietveld analysis suggests layered hexagonal structure [Figure 3.1(c)] and crystal structure is obtained with the cations/anions occupying interstitial positions.

Table 3.1 Parameters used to obtain fitting but failed

Space group	Wyckoff Positions	Element	x	y	z	Coordination
$R\bar{3}m$	3a	Cu	0	0	0	Cu, Pb octahederal
	3b	Pb	0	0	0.5	
	6c	I	0	0	±z	
$R3m$	3a	Cu	0	0	0	Cu, Pb octahederal
	3a	Pb	0	0	0.5	
	3a	I	0	0	0.25	
	3a	I	0	0	0.75	
$R3m$	3a	Cu	0	0	0	Cu octahederal, Pb prismatic
	3a	Pb	0	0	0.833	
	3a	I	0	0	0.416	
	3a	I	0	0	0.5833	
$R3m$	3a	Cu	0	0	0.833	Cu prismatic, Pb octahederal
	3a	Pb	0	0	0	
	3a	I	0	0	0.416	
	3a	I	0	0	0.5833	

In the structure, it is resembling a simple 2D layer structure where layer A (CuI), is related to the other two layers, B (I–I, triangular) and C (Pb–I) in a close-packed lattice through in-plane translations of (1/3, 2/3) and (2/3, 1/3) along the hexagonal cell vectors [Figure 3.1(c)].

Table 3.2 Parameters used to obtain fitting.

Space group	**Wyckoff Positions**	**Element**	**x**	**y**	**z**
$R\bar{3}m$	3a	Cu	0	0	0
	3b	Pb	0	0	0.51135
	18h	I	0.4489	-0.4489	0.51135
	18f	I	0.359	0	0
	18g	I	0.6832	0	0.5
	36i	I	0.1679	0.271	0.3336
	6c	I	0	0	-0.2062

The layers A, B and C are stacked periodically in a sequence AB1CB2AB3CB3AB2CB1A in 21R prototype representations where B represents inversion symmetry of layer B. The variation of lattice parameters with sintering temperature is plotted [Figure 3.1(d)]. It is observed that on increasing the sintering temperature, the lattice parameters increase for sintering temperature 30 ℃ . While, the lattice parameter ‘c’ is nearly constant (a plateau) when the sintering temperature is between 30 and 150 ℃. Further, grain size estimation is done using Image J software and SEM micrographs with grain size histograms as shown in Figure 3.4. Highest grain size observed in the sample sintered at 100 ℃ (in the plateau region) [Figure 3.1(e)]. This suggests that the grain size is c-axis determined (octahedral coordination).

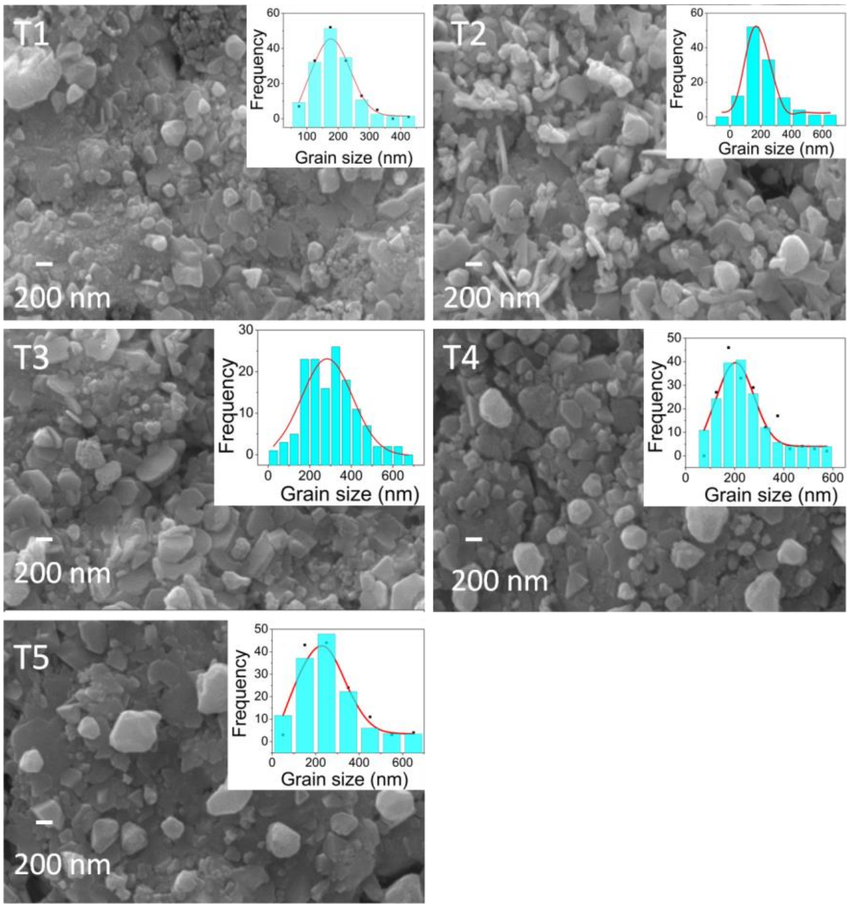

Figure 3.4 SEM micrographs and grain size histograms for the estimation of grain size.

3.3.2 Current-Voltage studies

The room temperature IV measurement of the $CuPbI_3$ samples sintered at different temperatures (T1–T5) are taken as per time scale shown in the figure 3.5(a). The scan rate is also believed to affect hysteresis due to ion migration[204][205][206]. In the present case, the objective of the work is to alter the microstructure at grain and grain boundary, resulting in different ion migration at the interface. Therefore, different samples showed different I–V hysteresis.In view of this, the variation of scan rate seems beyond the present context and the scan rate has been decided according to our previous work [207] where minimum hysteresis is observed at 1.66 V s^{-1} for $CsPbBr_3$ sample .

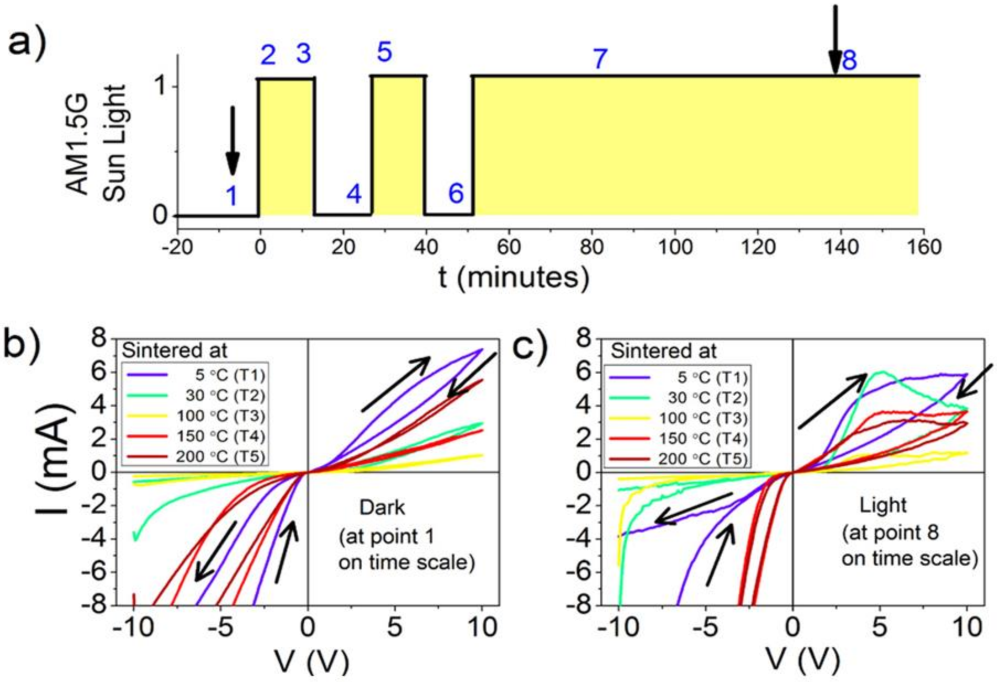

Figure 3.5 Time scale: AM 1.5G sun light applied to samples, the arabic numerical (1–8) represent the sequential point on time scale at which IV measurement has been taken. IV curves for sample sintered at 5, 30, 100, 150 and 200 ◦C (abbreviated as T1, T2, T3, T4 and T5 respectively) (b) in dark (point 1 on time scale) and (c) In light (point 8 on time scale).

We have studied the retention features with time for T2 and T3 samples as mentioned in Figure 3.5(a). The IV characteristics of sample (T1–T5) in dark (point 1 on time scale) condition and in light (with illumination of AM 1.5 G Sun light: point 8 on time scale) are plotted [Figure 3.5(b) and (c), respectively]. The voltage sweep is divided into 4 regimes: −10 V to 0 V (I), 0 V to 10 V (II), 10 V to 0 V (III), 0 V to −10 V (IV) where I and II belong to forward scans and III and IV belong to reverse scans. It is seen that in the 3rd quadrant [Figure 3.5(b) and (c)], the samples T1, T4 and T5 are showing conducting state while samples T2 and T3 current is almost independent of biasing state except for T1 in light. T1 sample in light shows conducting behaviour for forward scan while resistive features for reverse scan. However, the characteristic features are observed in 1st quadrant and explained thereafter.

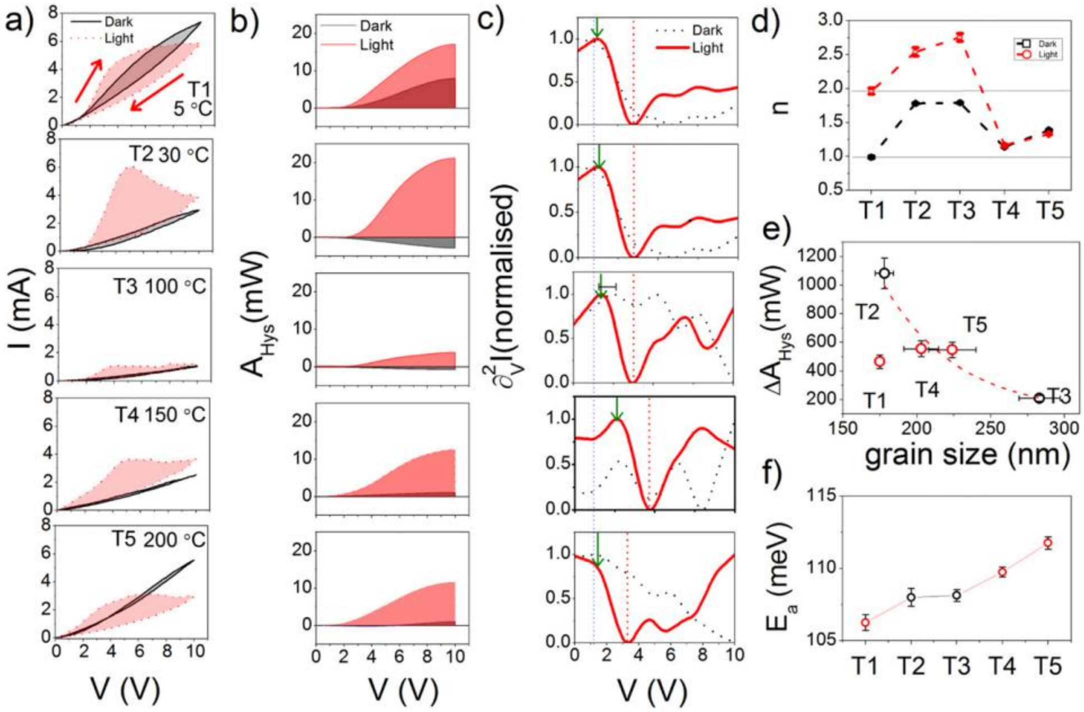

Figure 3.6 (a) The I–V curves for dark and just illuminated (b) AHys with voltage for the studied samples (c) second order derivative with voltage (d) variation of extracted parameters ‘n’ (lines are to guide only) from fitting $J = kE^n$ for both dark and light (e) variation of ΔA_{Hys} with the grain size (f) variation of activation energy with the sintering temperature.

The I-V characteristic curves in dark and light (with illumination of AM 1.5 G sun light), are compared for the $CuPbI_3$ samples sintered at different temperatures (T1–T5) [Figure 3.6(a)]. In light, I–V response possesses the feature similar to ferroelectric materials especially for sample T2, where a sharp rise in the current is observed. While, in dark, the hysteresis area is smaller rather resembling I-V curves for nonferroelectric materials as compared to I–V response in light [Figure 3.6(b)] for all samples under study [Figure 3.6(b)]. Further, the hysteric area decreases with increasing sintering temperature up to 100 ℃, thereafter an increase in hysteresis area is observed. For better understanding of the I–V characteristics features, we use the tunnelling spectroscopy [Figure 3.6(c)] for T1–T5 samples. Before the onset of current (marked by green arrow), some linear variation is observed which varies significantly from sample to sample as well as with light conditions. In general at low voltage, the I–V curve follows the Ohm's law, but in the present case except for T4, this feature is missing especially in case of light. However, first variation is observed at $\sim$1.2 V (marked by black dotted vertical line). The onset voltage systematically increases up to T4, there after it decreases. Interestingly, the onset voltage is almost same for dark and light for each sample, except T3 where the onset voltage decreases in light. Another characteristics feature is the switching voltage in light, beyond which exhaust behaviour appears, switching voltage also follows the similar trend as observed for onset voltage.

For further clarity, the I–V curve (up to switching voltage) is fitted with $I = kV^n$ is shown in Figure 3.7). The variation of extracted parameters 'n' for dark and light, is plotted [Figure 3.6(d)]. In both cases dark or light, the exponent 'n' increases up to T3 where maxima is observed. But, apart from the trend, another feature is value of 'n'. For T1, in dark the value is 1 and in light it is 2. It shows ohmic behaviour in dark and trap free behaviour up to switching voltage [208].

Similar difference in the dark and light is also observed for the sample T2 and T3. However in these two cases, in dark itself it is showing near to trap free behaviour and with light behaviour becomes (anomalous) resonant. In contrast, the sample T4 and T5 shows nearly ohmic behaviour and do not show any variation in the value of 'n' with light.

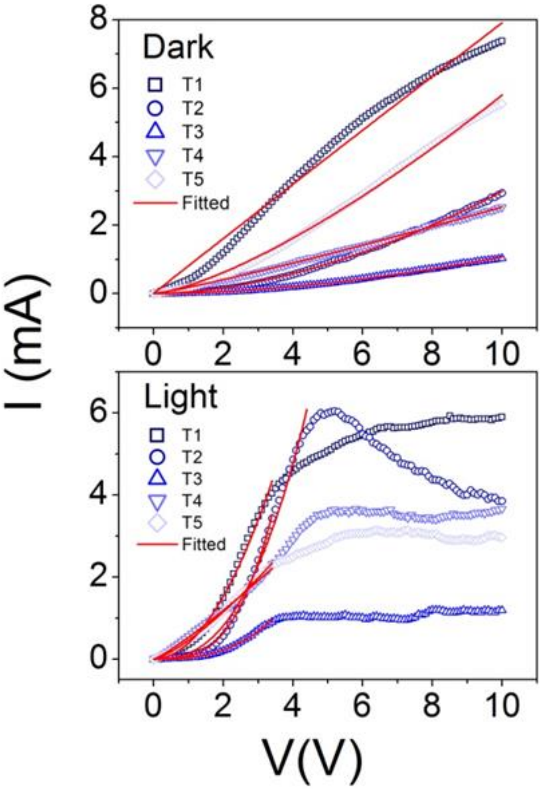

Figure 3.7 Fitting of I-V characteristics in dark and light with the relation $\mathbf{I} = \mathbf{kV^n}$

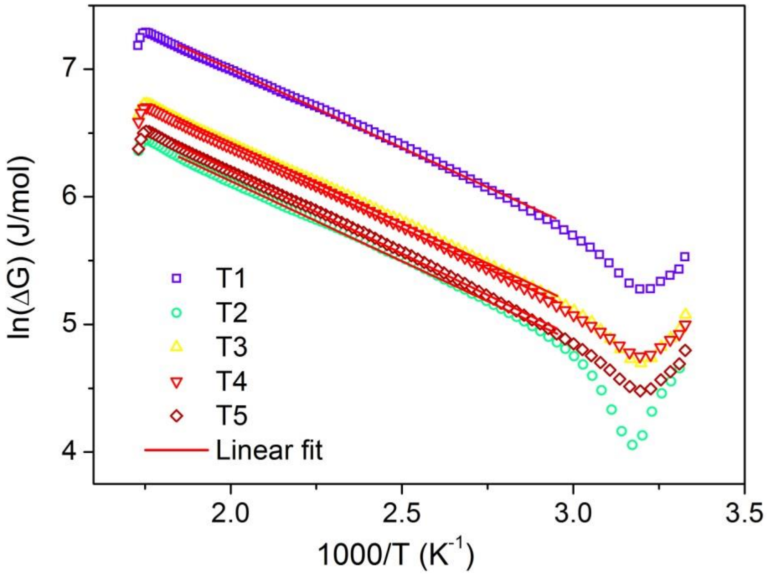

Figure 3.8 Arrhenius plots for estimation of activation energy using Gibbs' free energy.

Coming back to hysteresis behaviour, the difference in the area of hysteresis (light–dark), ΔA_{Hys} appears to decrease with the grain size [Figure 3.6(e)] and is minimum for T3 while maximum for T2.

Interestingly, T2 and T3 are the samples which shows resonant value of the exponent 'n'. We have estimated the activation energy [Figure 3.6(f)] from Gibbs free energy, estimated from the specific heat curves shown in Figure 3.8, using relation $G = G_0 \exp(-E_a/k_B T)$ and observed again a plateau for T2 and T3 sample. Further, the value is nearly 0.1 eV (105–115 meV) which suggests I_i and I_{Pb} defect formation [209]. These kind of defects are associated with mobile and trapped charges. The small activation energy suggests the possibility of shallow traps.

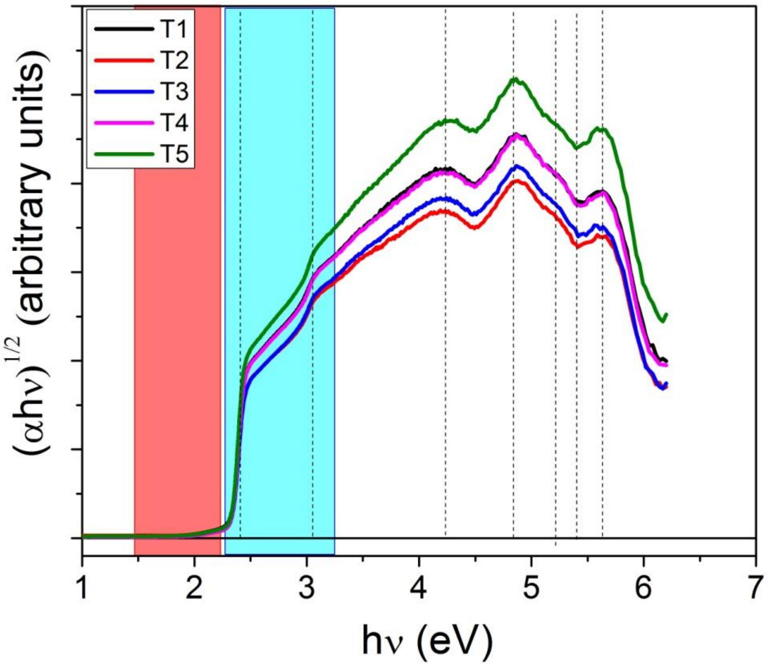

Figure 3.9 Band gap estimation using UV-visible spectroscopy.

The shallow traps at interface can be filled by field injected charge carriers. However, the photo injected charge charges can fill the shallow traps present at the bulk and interface. This fact is evident in Figure 3.6(d) where 'n' increases significantly indicating trap free behaviour with light as compared to dark photo current. In polycrystalline samples, the grain boundary volume significantly affects the trap density. Therefore hysteresis area significantly varies with grain size as seen in the Figure 3.6(e).

3.3.3 Impedance Studies

It is well known that the halides are ionic in nature and therefore possess localized charges which can hop to nearest neighbour vacant sites. To find the vacancy migration time in grains and grain boundaries, we have applied impedance spectroscopy before (pristine) and after photo exposure (after light).

In Figure 3.10(a) the impedance spectra (at ac voltage amplitude 1 V) for Pristine and light are compared. It can be seen that before illumination, grain and grain–boundaries are well defined. While, after illumination diffuse spectra is observed at low frequencies (grain–boundary).

Grain size significantly affects the impedance behavior of materials, by influencing charge transport and polarization mechanisms. In T5 sample, grain–boundary contribution diffuses before and after light with the increase in number of grain–boundaries and suggest interfacial polarization. Smaller grains increase the density of grain boundaries, which act as barriers to charge carriers due to their higher resistivity and capacitance. This results in higher impedance at grain boundaries, often dominating the overall response in materials with fine grains.

Conversely, larger grains reduce the grain boundary contribution, leading to lower overall impedance and higher conductivity. In addition, from Figure 3.8 we can clearly see the electronic contribution is not affected with the grain size as the band gap of the studied samples is nearly constant.

From Figure 3.6(f), we have observed that T2 and T3 possess almost similar activation energy and exponent 'n' in dark but nearly at extreme in terms of grain size and hysteresis area.

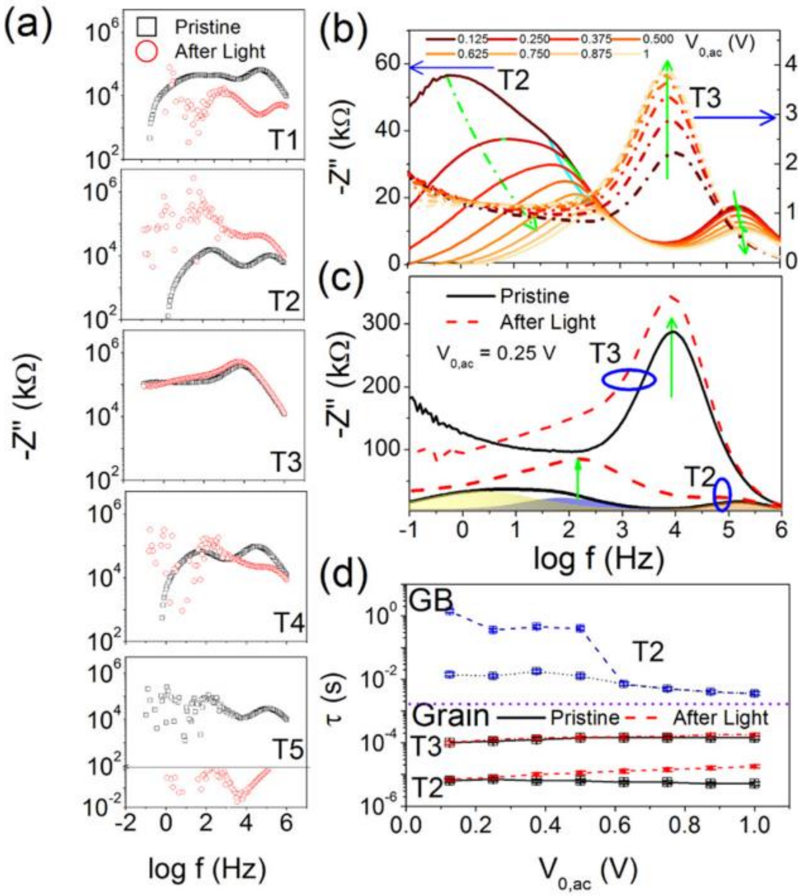

Figure 3.10 (a) Impedance spectra (for ac voltage amplitude 1 V) before and after light with the grain size showing disintegration of grain–boundary, (b) Bode plot of imaginary part of permittivity with the oscillation amplitude for T2 and T3 sample, (c) Gaussian fitting of T2 and T3 sample at small oscillation amplitude 0.25 V before and after light and (d) relaxation time for T2 and T3 sample before and after light in grain and grain–boundary regime.

In order to inspect the impact of microstructure on the photoconduction hysteresis, hereafter we are comparing T2 and T3. The Bode plot of T2 and T3 sample is studied with the various oscillation amplitudes from 1 mV to 1 V [Figure 3.10(b)]. However at low amplitude (<0.125 V) scattered data is obtained. It is seen that grain contribution of T3 sample is occurring at lower frequency than that of T2.

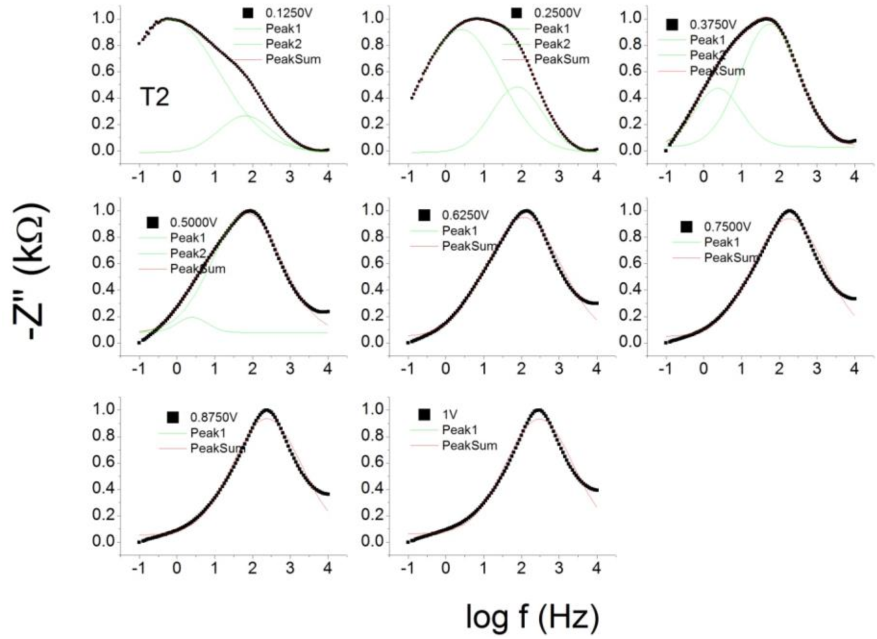

Figure 3.11 Fitting of Imaginary part of Impedance using Gaussian function with oscillation amplitude for T2 sample in dark.

Simultaneously, grain–boundary contribution of T3 is nearly parallel to frequency axis, whereas grain–boundary contribution in T2 sample is showing distribution of relaxation times as one kink and one maxima are observed [Figure 3.10(b)]. Further, the grain and grain–boundary regions are fitted with the Gaussian function, and seen that grain contribution consists of one peak while grain–boundary region is fitted with 2 peaks [Figure 3.10(c)] with voltage fitting of impedance spectra with Gaussian function is shown in Figure 3.11). However, we have tried for the number of peaks to find the maximum relaxation times but only two peaks are observed. But after illumination, we have observed single grain and grain–boundary peaks. Further, relaxation time for the grain and grain–boundary contributions of T2 and T3 sample is plotted in Figure 3.10(d). It is seen that in grain contribution of T2 sample, time is of the order of μs suggesting the migration of I^{-} ions at interstitial sites or at antisite[210] in the grain region before and after light. While at the grain contribution of T3 sample is showing the time of 10^{-4} s before and after light. The relaxation time value suggest the ion migration through hopping (hopping polarization). Further, grain–boundary contribution of T2 sample shows the time of tens of milliseconds to 1 s, suggesting the migration of Pb^{2+} ions [210] in interface region and after light grain–boundaries disintegrates. These relaxation times are also not altered with the oscillation amplitudes before and after light suggesting the hopping polarization as it is independent of the oscillation amplitudes.

3.3.4 Hopping (space charge) polarization

In order to understand the polarization (relaxation) behaviour, Figure 3.12(a) frequency dispersion (Bode) curve of relative real (ε') and imaginary (ε'') permittivity of T2 and T3 samples for both pristine and after light fall conditions, has been studied. A colossal value of permittivity at low frequency observed, which hints the presence of Maxwell–Wagner polarization for both the samples.

In case of T3, no significant variation is observed between pristine and after light fall cases. Although at low frequency (<105 Hz) ε'' is dominant in both cases suggesting defect (sluggish) formation. Further, the two permittivity functions are nearly parallel to each other at low frequencies (<10 Hz).

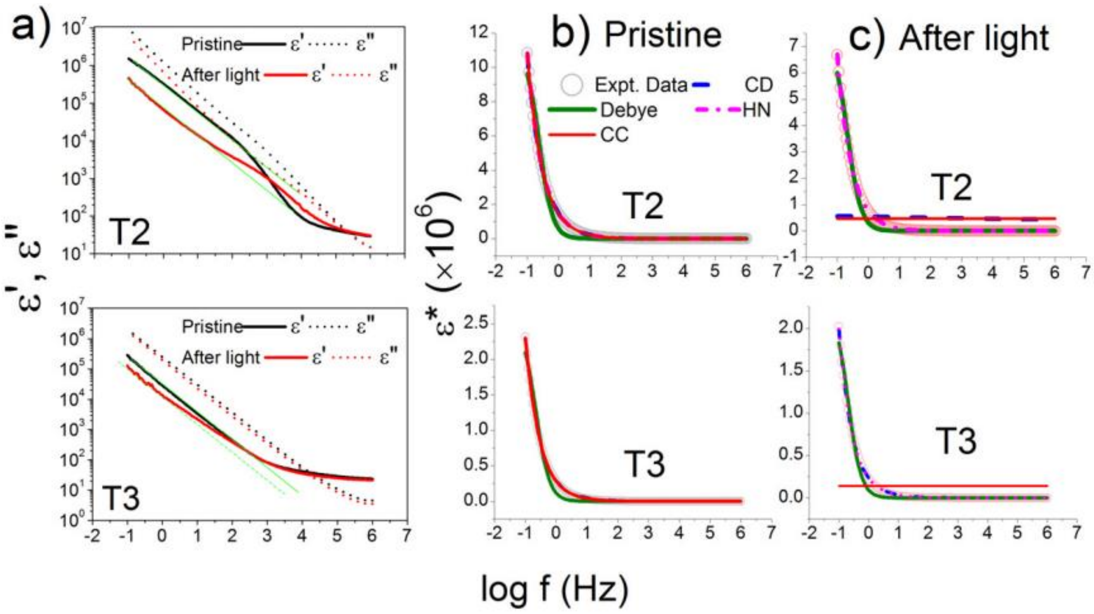

Figure 3.12 Frequency dispersion (relative) permittivity curves for the T2 and T3 samples in pristine and after light fall conditions.

In frequency regime ∽ kHz, a cross over between ε' and ε'' is observed suggesting space charge relaxation is appearing at higher value suggesting the orientational polarization. In the present case, although permittivity curves are not resolvable, but still in T2 sample the anomalous frequency dispersion is observed in the vicinity of space charge relaxation regime. In order to understand the relaxation distribution, we further fitted [Figure 3.12(b) and (c)] the complex relative permittivity ε^* using various relaxation models [debye, cole-cole) and Cole–Davidson (CD)] long with general Havriliak–Negami (HN) model [equation (3.1)] [211]. Here ε_{op}, ε_s, τ are the high frequency permittivity, low frequency permittivity and relaxation time respectively. The symmetric and asymmetric (loss peak) exponent parameter, α and β are fractional non negative numbers.

$$\frac{\varepsilon^* - \varepsilon_{op}}{\varepsilon_s - \varepsilon_{op}} = \frac{\varepsilon^* - \varepsilon_{op}}{\Delta\varepsilon} = (1 + (i\omega\tau)^{1-\alpha})^{\beta-1} \tag{3.1}$$

From the Figure 3.12 and Table 3.3 and 3.4, it can be concluded that in pristine condition T2 and T3 samples follow the Cole–Cole (CC) and Cole–Davidson (CD) response function respectively. However, after light fall, the relaxation mechanism is changed in the case of T2 sample. It is important to mention that value of asymmetric exponent β is negative.

Table 3.3 Relaxation parameters for pristine sample.

Model	**T2**					**T3**				
	α	**β**	**logτ**	**Δε x 10^6**	**R^2**	**α**	**β**	**logτ**	**Δε x 10^6**	**R^2**
Debye	0	0	-4.3(2)	1.14(4)	0.9723	0	0	-4.5(2)	2.52(8)	0.9780
Cole-Cole	0.2335(4)	0	-52(1)	76(2)	0.9999	0.218(1)	0	-23.8(8)	8.6(2)	0.9999
Cole-Davidson			Poor Fitting			0	0.260(2)	-13.02(30)	4.23(8)	0.9999
Havriliak-Negami	0.334(4)	-0.198(9)	206(22)	30(3)	1	0.000002(1)	0.260(0)	-13.02(0)	4.23(0)	1

Table 3.4 Relaxation parameters for sample after light fall

Model	**T2**					**T3**				
	α	**β**	**logτ**	**Δε x 10^6**	**R^2**	**α**	**β**	**logτ**	**Δε x 10^6**	**R^2**
Debye	0	0	4.7(2)	7.3(2)	0.9792	0	0	-4.9(2)	2.27(7)	0.9780
Cole-Cole			Poor Fitting					Poor Fitting		
Cole-Davidson			Poor Fitting			0	0.243(2)	14.2(4)	4.0(1)	0.9995
Havriliak-Negami	0.56(3)	-0.9(1)	486(218)	636(300)	0.9999	0.000003(1)	0.243(0)	14.25(0)	4.06(0)	1

Therefore in spite of good value of fitness co-efficient (R^2), we have to reject HN model too, for T2 sample. For the relaxation time estimation we have to rely on Debye model as value estimated from rest of three model are quite high and beyond any physical understanding. After light fall, T2 sample shows an anomalous increase in the relaxation time ($\sim10^5$ s). Although in the rest of three cases, it is almost in the same range (10^{-4} to 10^{-5} s) as estimated from impedance spectroscopy. The high value of $\Delta\varepsilon$ suggest space charge polarization in both samples.The space charge polarization slightly reduces after light fall conditions for T3 but increases for T2. We speculate interfacial polarization for T2 sample after light fall due to increase in space charge polarization and relaxation time. While, for the pristine T2 sample we expect an apolar dielectric behaviour as suggested by CC model .On the other hand, for pristine T3 sample, dipolar (due to hopping species) dielectric behaviour is suggested by asymmetric loss peak and the relaxation mechanism does not alter significantly for T3 sample after light fall. The loss asymmetricity $(1 - \beta)$ slightly increases and hopping relaxation occurs slightly earlier. Inquisitively, we have further studied the temporal plots (figure 3.13) before and after light (as grain boundary disintegrates) using differential impedance analysis and found that sample T2 is showing Warburg behaviour while T3 is capacitive in grain regime.

Further, hindrance is created at the interface of T2 sample while interface of T3 is highly resistive. The fractal exponent is estimated in bound capacitance model (BCP) using relation $|Z| = f^{-\alpha}$ is plotted in Figure 3.13. All the plots of $log\ |Z|$ vs $log\ f$ in Figure 3.14,3.15, 3.16 and 3.17, where $\alpha = 0$ for pure resistive, $\alpha = 1$ for pure capacitive and $\alpha = 0.5$ corresponds to diffusion limited bound transport in a layer.

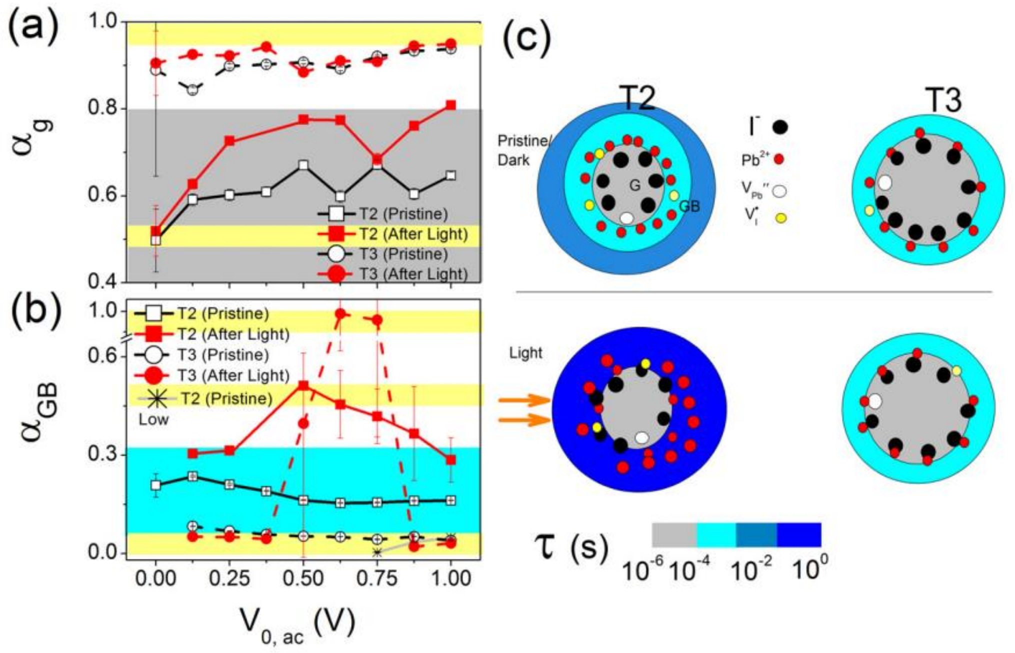

Figure 3.13 : Fractal exponent in BCP using relation $|Z| = f^{-\alpha}$ for (a) grain and (b) grain boundary of pristine and after light sample, where $\alpha = 0$ for pure resistive, $\alpha = 1$ for pure capacitive and $\alpha = 0.5$ corresponds to diffusion limited bound transport in a layer. However, $\alpha = 0.35$ describes the conduction with the hindrances of the host matrix and increase in the value of α from 0.5 to 0.8 suggest increased surface accumulation of charge carriers as illustrated by (c) scheme for the T2 and T3 samples in Dark and AM 1.5 G sun light

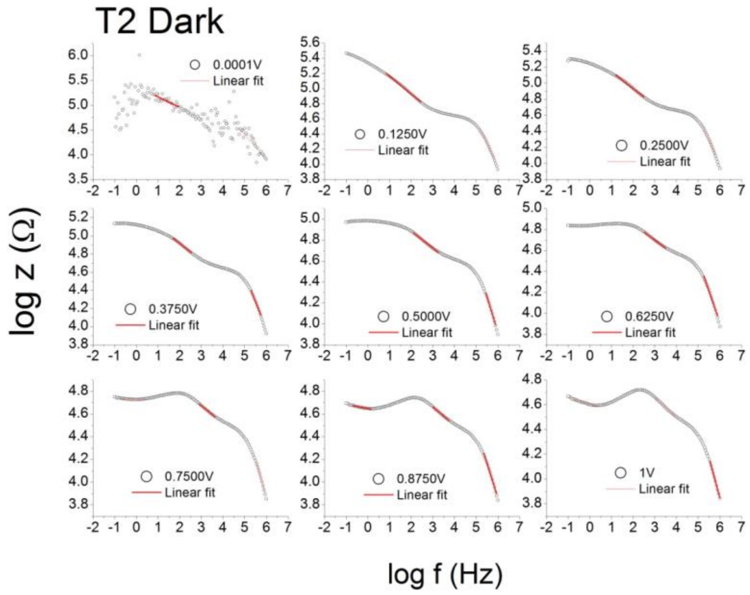

Figure 3.14 Plot of log|z| vs log f with oscillation amplitude for T2 sample in dark

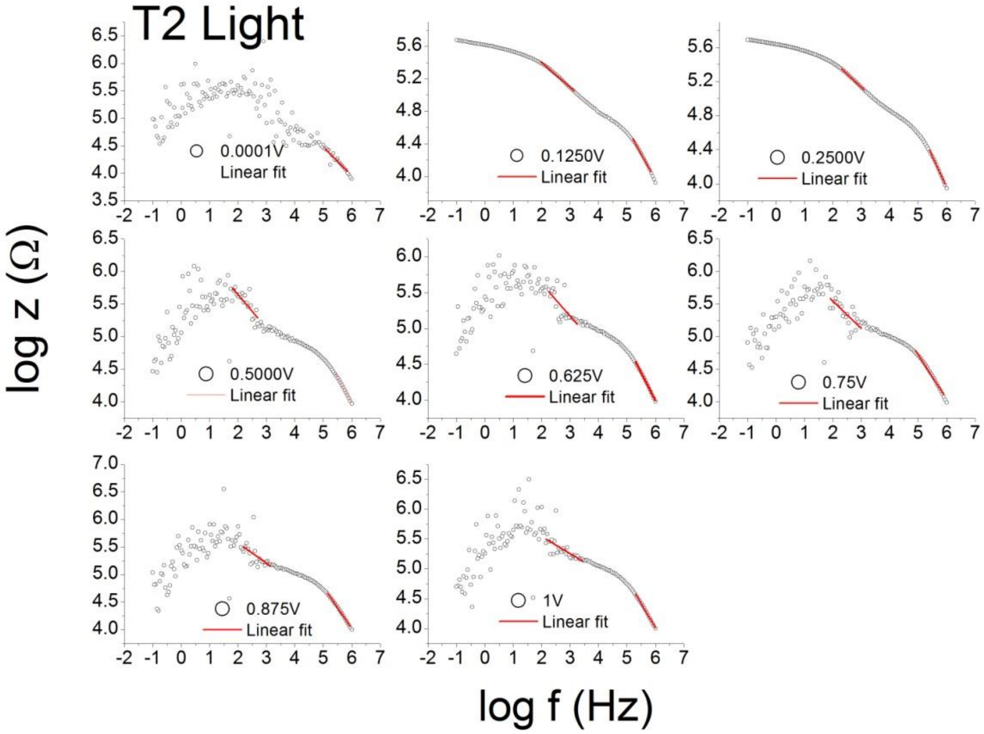

Figure 3.15 Plot of log|z| vs log f with oscillation amplitude for T2 sample in light

However, $\alpha = 0.35$ describes the conduction with the hindrances of the host matrix and increase in the value of α from 0.5 to 0.8 suggest increased surface accumulation of charge carriers [212]. In figure 3.13, it can be seen that grain is capacitive and grain boundary is resistive for T3 even after light fall. While, in T2 sample, charge accumulation occurs at grain surface, instead of hindrance for the motion of charge carriers created at the grain boundaries before light and after light charge carriers start accumulating at the surface and again creating hindrance with voltage. The summary of observation up to Figure 3.13(b) has been illustrated in Figure 3.13(c).

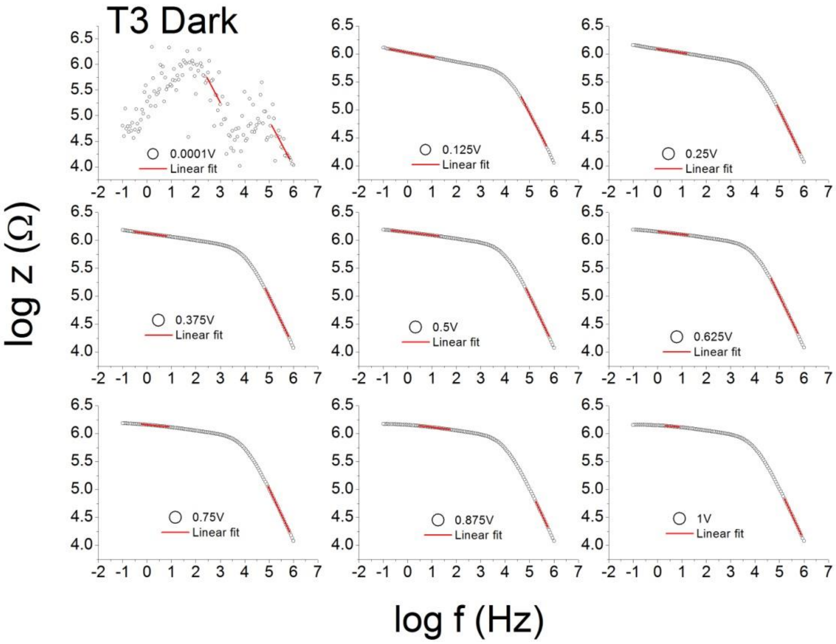

Figure 3.16 Plot of log|z| vs log f with oscillation amplitude for T3 sample in dark.

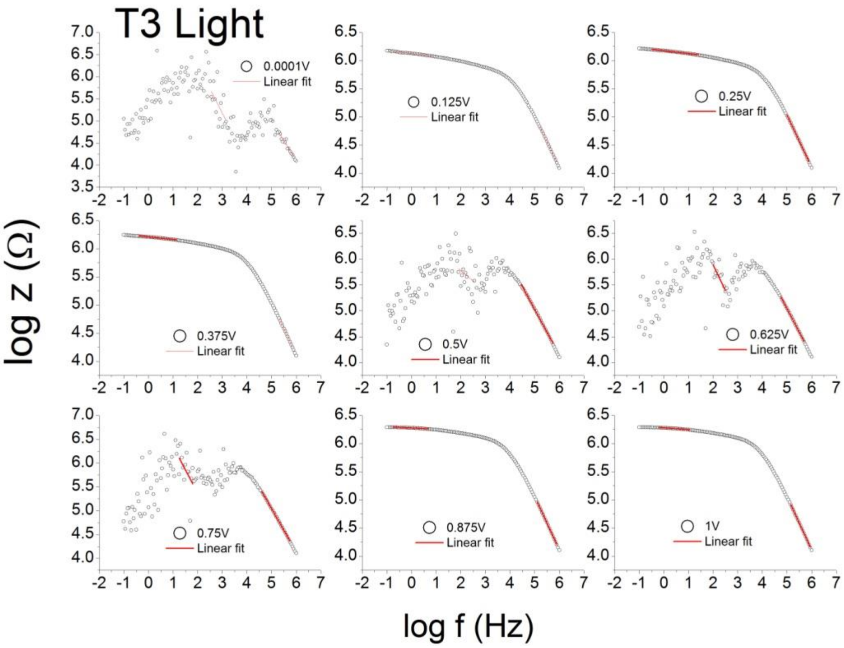

Figure 3.17 Plot of log|z| vs log f with oscillation amplitude for T3 sample in light.

3.3.5 Conduction mechanism

In Figure 3.6(c), we have observed the switching voltage and exponent 'n' in the I-V curve. Here, we are comparing the photoconduction behaviour of T2 and T3. Figure 3.18(a) shows Frenkel–Poole (FP) fitting and the relative dielectric constant estimated from Figure 3.18(b) from the slope of FP fitting using relation $ln\sigma_E\ \alpha\ \sqrt{(E/\varepsilon_r)}$ [208][213]. With photofield injection of charge carriers, the conductivity increases sharply due to increase in photogenerated charge carriers and mobility.

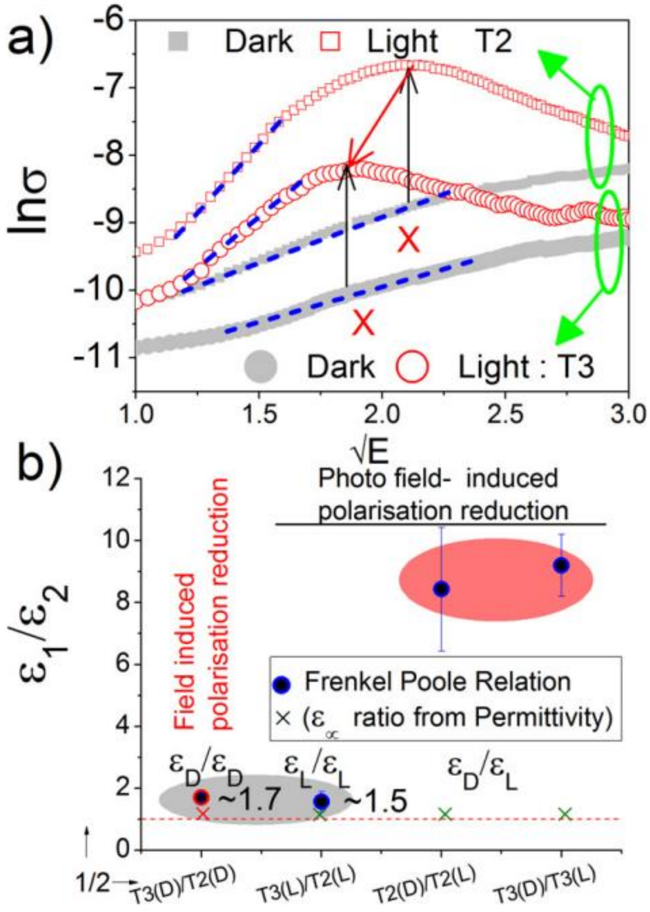

Figure 3.18 Frenkel poole curves and (b) variation of relative dielectric constant for the T2 and T3 samples in dark and AM 1.5 G sun light

The increase in mobility is evident by the critical field (E_C) peak [maxima corresponding to switching voltage see Figure 3.6(a)] for both samples which is absent for dark current. In case of dark current, conductivity rises continuously although with slight slower rates due to dynamics of field injected charge carriers and local field distortion by seathing at grain and GB interface. In case of photo current, E_C is smaller for T3 as compared to that of T2, therefore average mobility should be higher in T3 sample. In figure 3.18(b), it is observed that ratio of ε_r for T3 and T2 in dark (only field injected charge carriers from contacts) $\frac{\varepsilon_{\mathrm{T3(D)}}}{\varepsilon_{\mathrm{T2(D)}}} \backsim 1.7$ is slightly higher as compared to the case in light (photo-field injected charge carriers)

$\frac{\varepsilon_{\mathrm{T3(L)}}}{\varepsilon_{\mathrm{T2(L)}}} \backsim 1.5$. Although the ratio at high frequency permittivity (ε_α) obtained from Figure 3.12(a) does vary significantly and is close to 1. So it is bulk limited conduction in dark for both the samples. With photo-field charge injection coulomb screening decreases significantly for both samples ($\frac{\varepsilon_{\mathrm{T3(D)}}}{\varepsilon_{\mathrm{T3(L)}}} \backsim 9$ and $\frac{\varepsilon_{\mathrm{T2(D)}}}{\varepsilon_{\mathrm{T2(L)}}} \backsim 8$) and hence polarization reduction. However, this value is very different than ε_α, thus electrode limited thermionic emission is expected in case photo-field injection. Larger polarization reduction results in higher mobility for T3 sample though conductivity is less. It indicates lesser charge concentration in T3 sample as compared to T2.

3.4 Conclusion

In this chapter, IV hysteresis parameters are significantly altered by the grain size and photo injection in $CuPbI_3$ perovskite halide with $R\bar{3}m$ (centrosymmetric) symmetry. In general, higher grain size leads to higher polarization with the formation of dipoles. In the present case, T3 has higher grain size in comparison to T2 leading to the higher polarization with the formation of dipoles at the interface (excluding space charge polarization). This is further confirmed through the fitting of permittivity with CD model. While in case of T2, the permittivity data is being fitted with CC model suggesting it as a apolar dielectric and this means there is no formation of dipoles but charge carriers are there [214]. Additionally from thermogravimetric analysis, mass loss corresponding to I2 is higher for T2 as compared with T3. Therefore I^{-} vacancy will be more in case of T2. Further, through impedance analysis, relaxation time corresponding to grain is of the order of 10^{-6} s in case of T2 while grain contribution of T3 sample is showing the time of 10^{-4} s. While grain–boundary contribution of T2 sample shows the time of tens of milliseconds to 1 s. These values indicate the distribution of relaxation times over the grain and grain boundary interface. If $\tau < \tau_0$ (relaxation time), the defects did not get enough time to relax, and hence relaxation can be achieved through vacancy diffusion conduction mechanism [215], therefore migration species contribute to conductivity. The DIA and impedance spectroscopy collectively suggests the accumulation of I^{-} and Pb^{2+} at grain and GB, respectively in T2 sample. With the higher I^{-} vacancy in T2 and charge accumulation of I^{-} ion at grain, not only increasethe probability of vacancy diffusion conduction but also FP detrapping process. While, the grain is capacitive and grainboundary is resistive with the formation of dipoles at the interface of T3 sample. Thus, apolar dielectric behaviour for the pristine T2 sample and dipolar (due to hopping species) dielectric behaviour for pristine T3 sample is confirmed. The transport studies also suggest slightly higher coulomb screening for T3 leading to higher polarization and less conductivity. This dipolar dielectric behaviour leads to the minimum hysteresis in dark condition. With photo-field injection, the conductivity increases sharply for T2 in comparison to T3 while average mobility of T3 sample is higher. It indicates T2 sample possesses much higher photogenerated charge carrier concentration. Further, electrode limited thermionic emission is observed with the reduction in coulomb screening with photo injection which suggests the charge carriers at interface. The hysteresis observed is higher in case of T2 sample than T3. For the reasons lying behind hysteresis observed in light, post light treated samples are analysed and observed that grain is capacitive and grain boundary is resistive for T3 even after lightfall. While, in T2 sample, charge carriers start accumulating at the surface and again creating hindrance with voltage afterlight. This is also suggesting the migration of I^- ions at interstitial sites or at antisite [216] in the grain region through hopping (hopping polarization). After light fall, T2 sample shows ananomalous increase in the relaxation time ($\sim 10^5$ s). Althoughin the rest of three cases, it is almost in the same range(10^{-4} to 10^{-5} s) as estimated from impedance spectroscopy. The high value of $\Delta\varepsilon$ suggest space charge polarization inboth samples. The space charge polarization slightly reduces after light fall conditions for T3 but increases for T2. We speculate interfacial polarization for T2 sample after light fall due to increase in space charge polarization and relaxation time and the relaxation mechanism does not alter significantly for T3 sample after light fall. As Pb^{2+} vacancies start accumulating at the grain boundaries and don't permit I^- vacancies to move for conduction leading to the grain boundary passivation in T2 sample. Whereas, T3 sample comprises of pure resistive and capacitive combinations, hence grain–boundary passivation doesn't occur and hysteresis is minimal for T3 sample. The photo induced ferroelectric like I–V hysteresis behaviour is appearing due to the hopping migration of Pb^{2+} and I^- leading to interfacial polarization in the thin region of grain–boundary. The hysteresis is reported to be affected by reorientable dipoles with non-centrosymmetry instead of depolarization potentials[217] but in centrosymmetric $CuPbI_3$, change in polarization behaviour from apolar to orientable dipolar polarization affects the hysteresis and apolar material has highest hysteresis while orientable dipole material has minimal hysteresis. In summary, our work suggests current voltage hysteresis can be reduced significantly in the materials with orientable dipoles at grain/grain boundary interface without any change in photo-field induced polarization behaviour.